Long Spin Coherence Times of Nitrogen Vacancy Centers in Milled Nanodiamonds

B. D. Wood,[1, *] G. A. Stimpson,[1, 2] J. E. March,[1] Y. N. D. Lekhai,[1] C. J. Stephen,[1] B. L. Green,[1] A. C. Frangeskou,[1, †] L. Ginés,[3] S. Mandal,[3] O. A. Williams,[3] and G. W. Morley[1, ‡]

[1]*Department of Physics, University of Warwick, Coventry, CV4 7AL, United Kingdom*
[2]*Diamond Science and Technology Centre for Doctoral Training,*
University of Warwick, Coventry, CV4 7AL, United Kingdom
[3]*School of Physics and Astronomy, Cardiff University,*
Queen's Building, The Parade, Cardiff, CF24 3AA, United Kingdom
(Dated: March 31, 2022)

Nanodiamonds containing negatively charged nitrogen vacancy centers (NV^-) have applications as localized sensors in biological material and have been proposed as a platform to probe the macroscopic limits of spatial superposition and the quantum nature of gravity. A key requirement for these applications is to obtain nanodiamonds containing NV^- with long spin coherence times. Using milling to fabricate nanodiamonds processes the full 3D volume of the bulk material at once, unlike etching pillars, but has, up to now, limited NV^- spin coherence times. Here, we use natural isotopic abundance nanodiamonds produced by Si_3N_4 ball milling of chemical vapor deposition grown bulk diamond with an average single substitutional nitrogen concentration of 121 ppb. We show that the electron spin coherence times of NV^- centers in these nanodiamonds can exceed 400 μs at room temperature with dynamical decoupling. Scanning electron microscopy provides images of the specific nanodiamonds containing NV^- for which a spin coherence time was measured.

I. INTRODUCTION

The negatively charged nitrogen vacancy center (NV^-) in diamond [1] has attracted attention as a tool in quantum information [2, 3], magnetometry [4, 5], electrometry [6–9], and thermometry [10–13] using optically detected magnetic resonance (ODMR). This leverages the optical initialization and readout of the electron spin state of the NV^- center, along with the microwave resonance of the spin state transitions, to control the state of the NV^- center [14]. In nanodiamonds, the NV^- has potential applications in sensing within biological material as living cells can take in nanodiamonds and remain functional, allowing local sensing within cells [15–26]. Also, nanodiamonds containing NV^- have been proposed as a platform to probe macroscopic spatial superpositions [27–32] and the quantum nature of gravity [33–35]. These proposals require macroscopic spatial superposition states of the nanodiamonds involved, therefore, diamonds with a diameter on the order of 1 μm containing a single NV^- center are proposed. Along with large nanodiamonds, the electron spin coherence time, T_2, of the NV^- is a critical factor for these experiments. Dynamical decoupling techniques are used to suppress the dephasing of the NV^- spin state due to static or slowly changing fluctuations in the environment, maximizing the T_2 time.

In bulk diamond, NV^- T_2 times exceeding 1 s have been observed, using dynamical decoupling, at cryogenic temperatures [36, 37]. At room temperature the longest NV^- T_2 time is around 2 ms using ^{12}C purification and dynamical decoupling [37, 38]. However, observed T_2 times in nanodiamonds are significantly shorter. The longest reported T_2 in micro- or nanodiamonds is 708 μs with dynamical decoupling and using isotopically pure ^{12}C diamond material that is etched into pillars of diameters 300 to 500 nm and lengths 500 nm to 2 μm [39]. For natural abundance ^{13}C micro- or nanodiamonds, the longest T_2 time reported for particles fabricated using etching techniques is 210 μs [40] and by milling 67 μs [41].

The T_2 time is sensitive to the dynamics of spins surrounding the NV^-, hence the shorter times for nanodiamonds containing uncontrolled ^{13}C spins. Therefore, it has been suggested that the suppression of NV^- T_2 in nanodiamonds is due to defects at the surface [42–44].

Here, we show that chemical vapor deposition (CVD) grown diamond with natural ^{13}C abundance and nitrogen concentration < 1 ppm, can be processed by milling to fabricate nanodiamonds containing NV^- with T_2 exceeding 400 μs at room temperature. Milling conveniently permits the creation of nanodiamonds from the full 3D volume of the bulk material at once, unlike etching. The nanodiamond T_2 measurements were carried out using confocal fluorescence microscopy (CFM), and the same nanodiamonds were viewed by scanning electron microscopy (SEM).

Single-crystal CVD diamond was manufactured by Element Six with an average single substitutional nitrogen concentration of 121 ppb measured by electron paramagnetic resonance [46], and a natural abundance of ^{13}C. The expected grown-in NV^- concentration was 0.4 ppb [47]. Prior to Si_3N_4 ball milling [48] the diamonds used for this research were irradiated with 4.5 MeV electrons for one minute and annealed for three hours at 400 °C, four hours at 800 °C and two hours at 1200 °C, similarly to previous methods [46, 49]. The irradiation time was chosen such that the expected final NV^- concentration

------

[*] ben.d.wood@warwick.ac.uk
[†] Current address: Lightbox Jewelry, Orion House, 5 Upper St. Martins Lane, London, WC2H 9EA, United Kingdom
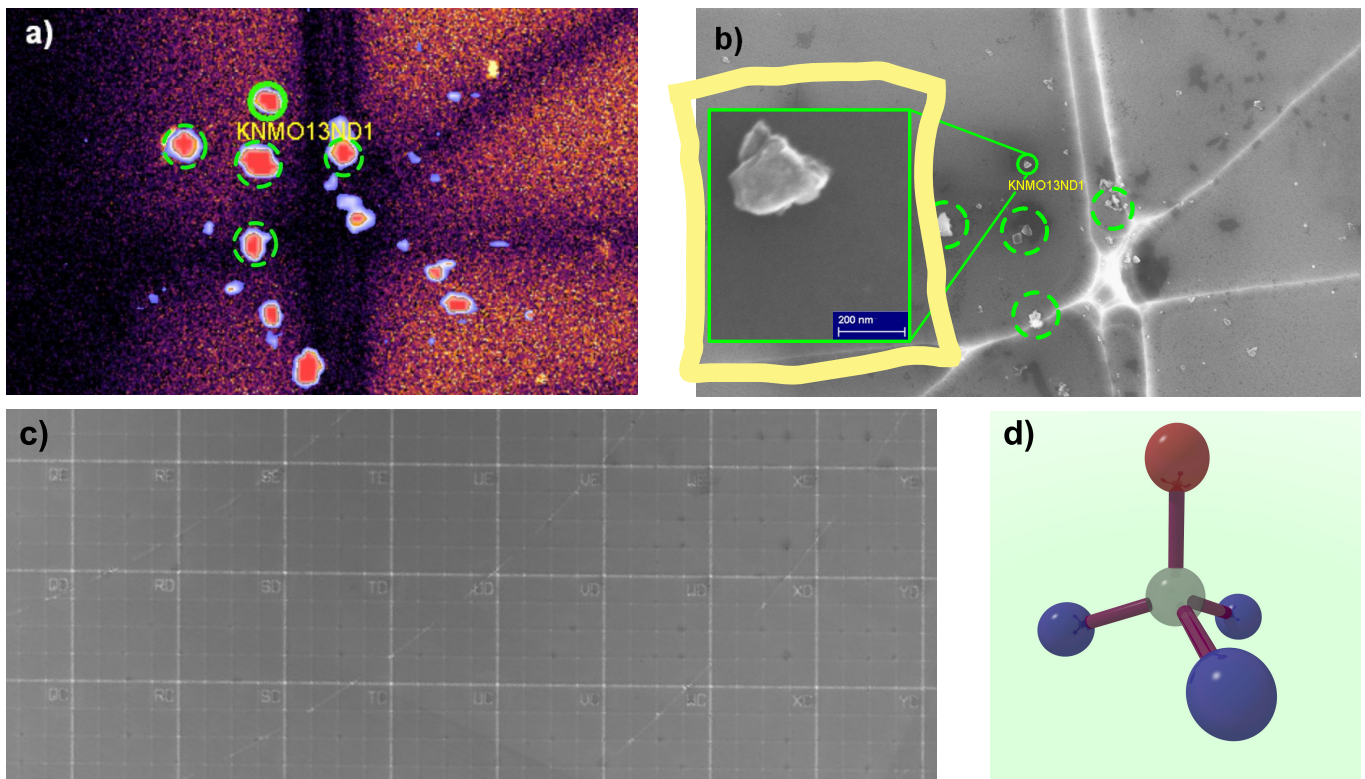[‡] gavin.morley@warwick.ac.uk

FIG. 1. (a) Confocal fluorescence microscopy (CFM) image, in red and blue (lighter grayscale), of nanodiamond KNMO13ND1 (ND1) overlaid onto a reflection image, in purple and orange (darker grayscale), of the grid-marked silicon. Image plotted using the Qudi software suite [45]. ND1 is identified by the solid green (gray) ring. The dashed green (gray) rings around nearby features are overlaid on both (a) and (b) which, along with the grid, verify that the CFM and scanning electron microscopy (SEM) are both viewing the same nanodiamonds. (b) SEM imaging of the same area in (a) is necessary to provide a measurement of size. The inset shows a higher magnification image of ND1. (c) A lower magnification SEM image of an etched silicon map before nanodiamonds are introduced. Vertical and horizontal grid lines are visible along with arcs that are centered on the center of the silicon map. The grid lines visible in (a, b) are the intersection of horizontal, vertical, and arc markings. In (a) the grid lines are the dark lines to the right of ND1, and in (b) the grid lines are the bright lines to the right of ND1. Each small square has dimensions 25x25 µm. (d) NV$^-$ center schematic, three carbon atoms shown in blue (dark gray) at the bottom, one nitrogen in red (gray) at the top, and the transparent (light grey) central sphere is the vacant lattice site.

was approximately 1 ppb. Given the atomic density of diamond (1.77×10^{23} cm^{-3}), it was expected that a nanodiamond containing a single center was around 230 nm in diameter.

Ref. [48] provides a detailed report of the fabrication process, x-ray photoelectron spectroscopy measurements of the surface, and particle size distributions. In summary, the diamond plates were milled with Si$_3$N$_4$ balls to avoid magnetic contaminants from steel ball milling. After milling, the sample was acid cleaned in H$_3$PO$_4$ and then cleaned in NaOH, to remove the Si$_3$N$_4$ contaminants. This process does not remove all the Si$_3$N$_4$ contaminants, as the diamond sample gains mass after milling. The nanodiamonds were then annealed in an air atmosphere, dispersed in water and centrifuged at a relative centrifugal force of 40×10^3 g. The air anneal produces nanodiamonds that have surfaces consisting of C-Si, COOH, C=O, C-O, C=C, and C-C bonds.

The nanodiamonds were held in a suspension of methanol at a density of approximately 1 mg ml^{-1} and sprayed for three seconds by a nebulizer (Omron MicroAIR U22) into an upturned vial, ensuring that a high density of nanodiamonds were injected. The nanodiamonds were then allowed to precipitate onto silicon wafers. This was to reduce the 'coffee-ring' effect which was often observed in drop casting and to prevent aggregation which was found to be prevalent when using direct spray application. Other methods have also been demonstrated previously for mitigating the 'coffee-ring' effect [50]. n-type silicon wafers doped with 1×10^{15} cm^{-3} of phosphorus were plasma etched using photolithography to create a grid system for locating individual nanodiamonds. This allows verification that the same nanodiamond is being addressed in both the CFM and SEM measurements.

Under CFM, nanodiamonds containing single NV$^-$ centers were identified by Hanbury Brown-Twiss (HBT) measurements. HBT measurements quantify the degree of correlation between photon detection events for different time delays, $g^{(2)}(\tau)$. A single NV$^-$ cannot emit two

photons simultaneously, therefore $g^{(2)}(0) = 0$ is expected. However, background fluorescence generates spurious coincidence events so that $0 \leq g^{(2)}(0) < 0.5$ indicates a single center. Background counts are not subtracted from the HBT data in this work.

Those that displayed ODMR were selected and an external magnetic field aligned to the NV^- axis. The magnetic field is generated by a permanent magnet on an arm connected to three motors. Two motors rotate the magnet about perpendicular axes that intersect at the position of the sample. These allow rotation in a sphere around the sample without altering the distance between the magnet and the sample. The final motor linearly alters the distance between the magnet and the sample, without changing the angle. Therefore the angular alignment and magnetic field strength can be varied precisely and independently. To align the magnetic field, the fluorescent count rate is monitored and the angle of the magnet adjusted until the magnet can be brought close to the sample without the count rate decreasing. The count rate decreases in the presence of a misaligned field as the $m_s = 0, \pm 1$ levels are no longer eigenstates of the system and so the spin states mix [4]. ODMR could have been used for the magnetic field alignment, however we found that monitoring the count rate provided a faster alignment. For aligned NV^- centers the fluorescence intensity remains constant as the magnitude of the magnetic field increases [4]. Spin-echo decay experiments were then carried out at room temperature to determine T_2 times using the Hahn echo, XY8-1 and XY8-4 dynamical decoupling pulse sequences. The sizes of individual nanodiamonds were measured by SEM, as shown in Fig. 1.

II. RESULTS AND DISCUSSION

An automated survey collected HBT and fluorescence intensity measurements from 175 nanodiamonds containing NV^-, as shown in Fig. 2(a). Of the nanodiamonds measured, 34% contained a single NV^- center whilst 19% contained two, 16% contained three, and 31% contained more than three NV^- centers respectively. We have characterized $0 \leq g^{(2)}(0) < 0.5$ to indicate a single center, $0.5 \leq g^{(2)}(0) < 0.67$ indicates two, $0.67 \leq g^{(2)}(0) < 0.75$ indicates three and $g^{(2)}(0) \geq 0.75$ indicates more than three. The survey was conducted at an excitation laser power of $0.4 \, \mathrm{mW}$.

The sites marked to be included in the HBT survey were identified from their fluorescence under CFM, therefore the number of nanodiamonds that do not contain any NV^- centers was not measured. If Poissonian statistics are assumed for the number of nanodiamonds containing one, two, and three NV^- centers, a fit of $e^{-\lambda}\lambda^x/x!$ gives $\lambda = 1.5 \pm 0.3$. Therefore, it can be estimated that the number of nanodiamonds containing zero NV^- in the surveyed region is 40 ± 12. However, there are a number of factors that suggest that the data is not well described

by Poissonian statistics and that the number of nanodiamonds containing zero NV^- centers is an order of magnitude estimate at best. Firstly, whilst NV^- centers may have been incorporated into the bulk diamond material at an approximately constant rate, a range of nanodiamond sizes exist in the sample. Furthermore, selection bias exists in marking sites for survey. Bright, roughly circular, isolated fluorescence spots are more likely to be identified as a nanodiamond containing NV^- and marked for survey than a dim spot, or an extended patch of fluorescence.

Figure 2(a) also contains a number of single NV^- centers with unusually high fluorescence intensity. We typically see single emitters with $< 100\mathrm{kcts/s}$ under CFM, however an number of surveyed sites exceeded this with one approaching $200\mathrm{kcts/s}$. A possible explanation for the inflated fluorescence intensity is that the geometry of the milled nanodiamond, and location of the NV^- center are, by chance, in the required orientation to act as a waveguide [51, 52]. This could couple more of the emitted fluorescence into the microscope objective than would be the case from a spherical nanodiamond, boosting the measured fluorescence intensity.

HBT measurements on the nanodiamond labelled KNMO13ND1 (ND1) in Fig. 1 gave the value $g^{(2)}(0) = 0.39 \pm 0.02$, as shown in Fig. 2(b), indicating that it contained a single NV^- center. (For further discussion of this inflated $g^{(2)}(0)$ see Appendix B). SEM observations of ND1 were used to estimate that the maximum distance an NV^- center could be from the surface (R_{max}) was 106 ± 2 nm.

Spin-echo decay measurements were performed on seven nanodiamonds containing a single NV^- that also displayed satisfactory ODMR contrast (the difference in fluorescence intensity for an NV^- in the $m_s = 0$ or the $m_s = \pm 1$ states). The nanodiamond ND1 provided the longest T_2 time of all nanodiamonds measured, as shown in Fig. 3(a), with values of $T_2^{\mathrm{HE}} = 177 \pm 24$ µs, $T_2^{\mathrm{XY8-1}} = 323 \pm 21$ µs, and $T_2^{\mathrm{XY8-4}} = 462 \pm 130$ µs for the Hahn echo, XY8-1, and XY8-4 pulse sequences respectively. These measurements were taken at an external field strength, measured by ODMR, of $27 \, \mathrm{mT}$. Schematics of the pulse sequences are shown in Fig. 3(b).

T_2 measurements taken on the same nanodiamond before and after SEM indicated that the T_2 was not corrupted. Whilst small variations were observed, this is likely to be due to small changes in the magnetic field alignment [53, 54]. As discussed in section I, the nanodiamond surface is largely oxygen terminated [48]. Any oxygen based groups that may be removed under SEM will immediately return on venting. The only significant change to the sample after SEM is that background fluorescence increases. We suggest that this is due to electrostatic charging of the silicon under SEM, which then attracts more fluorescent material after venting. This increase in background fluorescence can be seen in Appendix B.
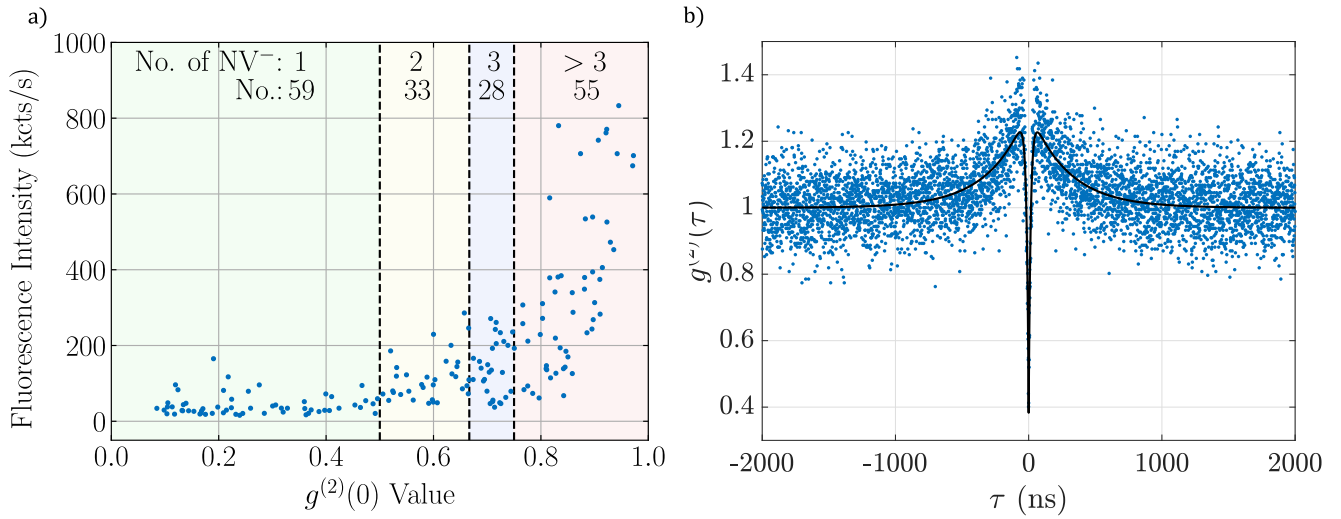
The measurements in Fig. 3(a) were made with the

FIG. 2. (a) Fluorescence intensity against $g^{(2)}(0)$ value. $0 \leq g^{(2)}(0) < 0.5$ indicates a single center, $0.5 \leq g^{(2)}(0) < 0.67$ indicates two, $0.67 \leq g^{(2)}(0) < 0.75$ indicates three and $g^{(2)}(0) \geq 0.75$ indicates more than three. A total of 175 nanodiamonds containing NV$^-$(s) were surveyed. (b) An example Hanbury Brown-Twiss (HBT) measurement of photon correlation for ND1. The black curve is a fit to $1 - a \left[b \exp \left(-\frac{|\tau|}{c} \right) + (1 - b) \exp \left(-\frac{|\tau|}{d} \right) \right]$, where $g^{(2)}(0) = 1 - a$. For this plot $g^{(2)}(0) = 0.38 \pm 0.04$. After multiple measurements, the value quoted in the text of $g^{(2)}(0) = 0.39 \pm 0.02$ is reached.
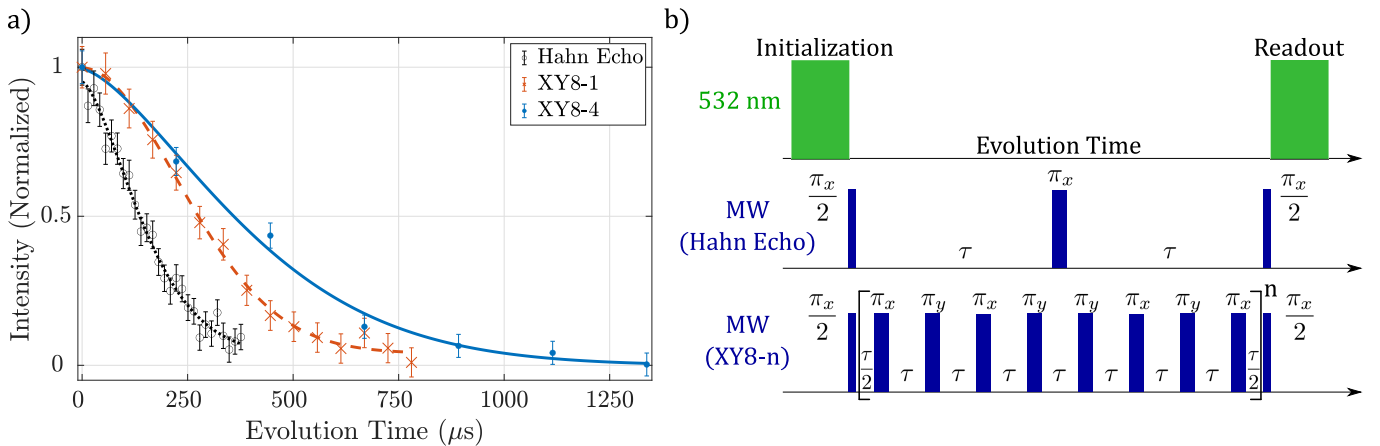

FIG. 3. (a) Spin-echo decay measurements of ND1. For the Hahn echo, XY8-1, and XY8-4 pulse sequences we measure coherence times $T_2^{\mathrm{HE}} = 177 \pm 24$ µs, $T_2^{\mathrm{XY8\text{-}1}} = 323 \pm 21$ µs, and $T_2^{\mathrm{XY8\text{-}4}} = 462 \pm 130$ µs respectively. Lines fit by $a + b \exp\left[-(t/T_2)^n \right]$. (b) The 532 nm laser and microwave (MW) pulses applied for the Hahn echo and XY8-n sequences. The bracketed block in XY8-n is repeated n times.

time delay between microwave pulses chosen to sample the peaks of the ^{13}C revivals of the spin-echo signal [53, 55] that is present in ND1 (see Appendix C). This allows the data to be fit by an exponential without sinusoidal components.

Hahn echo measurements on six other nanodiamonds containing single NV$^-$ gave T_2^{HE} in the range 3.3 to 53 µs, as shown in Fig. 4. The mean T_2^{HE} time, including ND1, was $\langle T_2^{\mathrm{HE}} \rangle = 51$ µs. From SEM imaging of this group, including ND1, the mean size was characterized by $\langle R_{\mathrm{max}} \rangle = 83$ nm. The six measurements were taken with external magnetic fields, measured by ODMR, that ranged from 26 to 50 mT.

The T_2 times presented here are, to our knowledge, the longest T_2 times for NV$^-$ centers in nanodiamonds with a natural abundance of ^{13}C, despite these nanodiamonds being produced by milling. Milling produces much larger quantities of nanodiamonds as it allows for production of nanodiamonds from the full volume of the bulk material, unlike etching. Previous measurements in the literature have reported that milled nanodiamonds contain NV$^-$ with T_2 times shorter than those in nanodiamonds produced by etching [40, 41]. Furthermore, we have introduced a technique with SEM and silicon grid mapping to image the exact nanodiamonds for which we measure NV$^-$ spin coherence times. Previous experiments
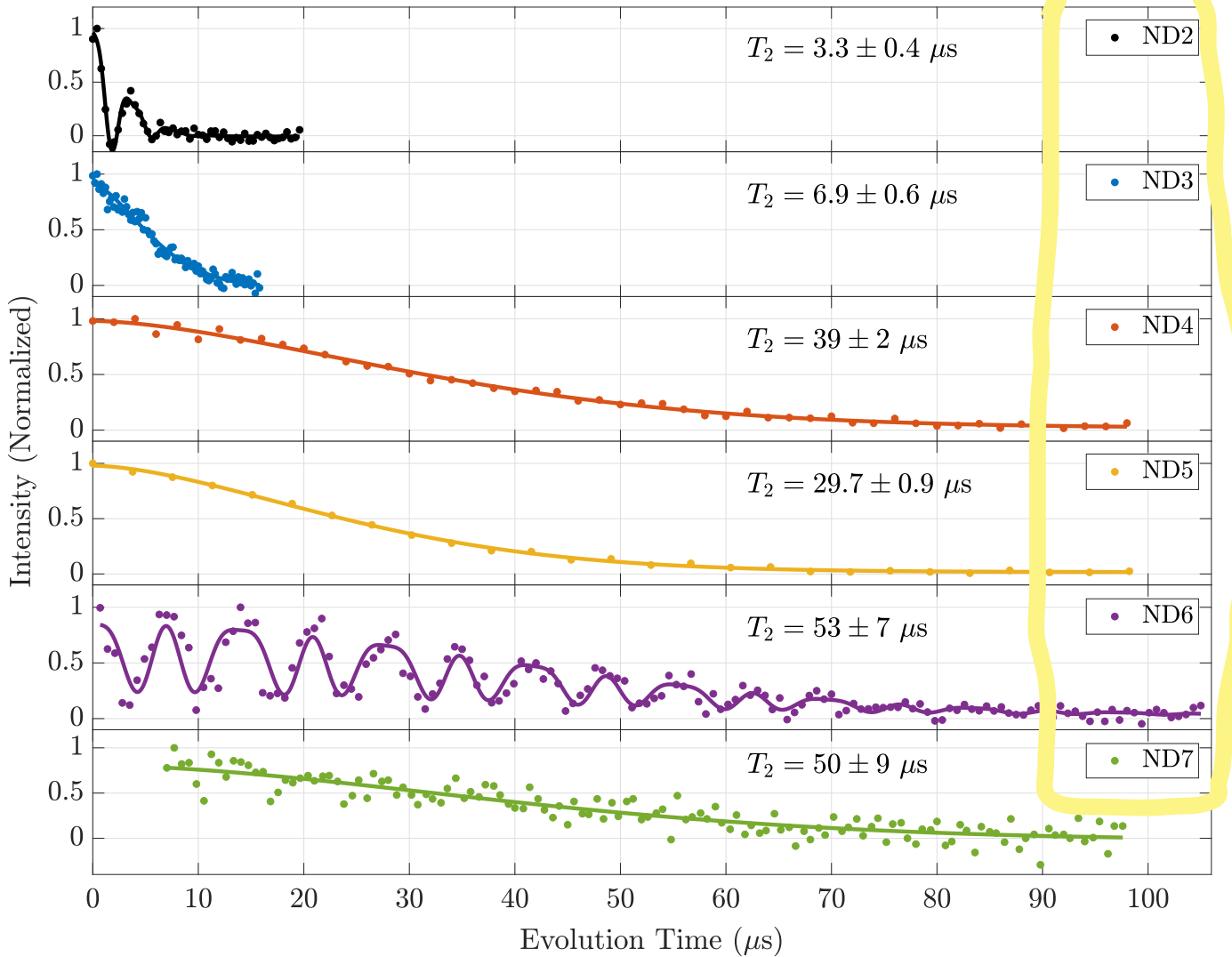
FIG. 4. Hahn echo measurements on six nanodiamonds other than ND1 containing single NV^-. Error bars are not shown as they are smaller than the data points. Dashed lines fit by $a + b\exp\left[-(t/T_2)^n\right]$ or, for those figures that contain ^{13}C revivals, $a + b\exp\left[-(t/T_2)^n\right]\left(1 - c\sin\left(\frac{\pi t}{d}\right)^2\sin\left(\frac{\pi t}{g}\right)^2\right)$ [53, 55]. For the plots with revivals the periods are as follows, for ND2: $d = 3.6 \pm 0.2$ µs, $g = 4.0 \pm 0.3$ µs, and for ND6: $d = 6.96 \pm 0.05$ µs, $g = 13.9 \pm 0.1$ µs.

reporting the T_2 time of nanodiamonds did not have a way of getting SEM images of the specific nanodiamond for which they measured spin coherence. Our T_2 time of 460 µs is over twice as long as the 210 µs reported in Ref. [40] using etching and over six times longer than the 67 µs reported in Ref. [41] with milling. Five of the six Hahn echo T_2 times in Fig. 4 are longer than the longest Hahn echo T_2 times previously reported for milled nanodiamonds of 2 to 6 µs in Ref. [41]. It should be noted that the nanodiamond pillars in Ref. [40] are of a similar size to those measured here, with diameter 50 ± 15 nm and height 150 ± 75 nm. However, in Ref. [41] the nanodiamonds are smaller, with the majority of diameters within 10-35 nm.

The nanodiamonds surveyed for Fig. 2(a) were in a different region on the silicon grid to those nanodia-

monds that were measured for spin coherence times. We estimate that around 80 nanodiamonds containing single NV^- centers were investigated to measure seven T_2 times. There are a number of reasons why a single NV^- may not produce a T_2 measurement. For instance, if the ODMR contrast is too low, the number of measurement repeats required to reach an acceptable signal-to-noise ratio becomes prohibitive. NV^-s can display low ODMR contrast if they are too far from the wire delivering microwave excitation, and we have also observed that some NV^-, even if close to the wire, have little to no ODMR contrast. This lack of ODMR contrast has been observed before [56]. NV^-s can also fail to produce a T_2 measurement due to the limited range of motion of the arms that align the magnet to the NV^- axis to avoid crashing into the sample stage. If the magnet cannot be aligned to

the NV$^-$ axis, then a magnetic field cannot be applied to break the degeneracy of the $m_s = 0, \pm 1$ levels without also significantly degrading the T_2 time [53, 54].

Under the assumption that all the nanodiamonds are spherical, and the NV$^-$s are located at the center of the sphere, we would expect that larger nanodiamonds would correlate with longer T_2 times. The further the NV$^-$ is from the surface, the decohering effects of the surface are suppressed. However, in practice our milled nanodiamonds are far from spherical, and the NV$^-$ center could be anywhere within the volume of the nanodiamond. As such, we do not observe a correlation between the size of the nanodiamond and the T_2 time (see Appendix D).

III. CONCLUSION

We observed a nanodiamond containing a single NV$^-$ electron spin coherence exceeding 400 µs, with dynamical decoupling. For other nanodiamonds containing single NV$^-$ centers, the average T_2 time measured by the Hahn echo sequence across the sample was 51 µs. All spin coherence measurements were performed at room temperature. The nanodiamonds containing NV$^-$ were fabricated from CVD diamond bulk material by Si_3N_4 ball milling [46, 48]. CVD allows diamond to be grown with low, and controllable, defect concentrations and milling permits the conversion of the entire bulk sample into nanodiamonds quickly, unlike masked etching of pillars. We have also used etched grid markings in silicon to be able to address specific nanodiamonds, that provided T_2 measurements, under SEM.

These T_2 times demonstrate that nanodiamonds produced by milling can contain NV$^-$ centers with T_2 times that are comparable with or longer, than those produced by etching. These T_2 times should enable AC magnetometry with a sensitivity on the order of $100\,\mathrm{nT\,Hz^{-1/2}}$ [4]. Furthermore, the high-volume fabrication enabled by milling is compatible with applications such as sensing [15–26] and nanodiamond levitation [27–31, 34, 35, 46, 57–62].

Appendix A: Electron Irradiation

The irradiation was performed by Synergy Health in Swindon, UK. The beam is not well characterized, however the beam current is approximately $20\,\mathrm{mA}$ and produces vacancies at a rate of around 0.3 ppm/hr. Based on prior experience of using the irradiation facility, the one minute exposure time was chosen such that the expected final NV$^-$ concentration was approximately 1 ppb.

Appendix B: ND1 photon autocorrelation

HBT measurements on ND1 gave a fitted autocorrelation value of $g^{(2)}(0) = 0.39 \pm 0.02$. Whilst this satisfies the $g^{(2)}(0) < 0.5$ condition for a single NV$^-$, it is larger than the values we typically observe for single NV$^-$ in nanodiamonds at room temperature. The inflated $g^{(2)}(0)$ value could be caused either by ND1 containing two NV$^-$ centers with the emission intensity of one suppressed, or ND1 contains a single NV$^-$ with a high background count rate, as background counts are not subtracted from the HBT data.

The first potential cause for emission suppression is if the two NV$^-$ have different orientations in the diamond lattice then the input polarization of the $532\,\mathrm{nm}$ excitation could couple preferentially with one orientation over the other. However, a number of experimental observations suggest that if there are two NV$^-$ then they have the same orientation. Firstly, there is only one pair of peaks observed in ODMR when an external magnetic field is applied. Secondly, a magnet can be aligned and moved from a distance of approximately $30\,\mathrm{mm}$ to approximately $5\,\mathrm{mm}$ from ND1 without changing the emitted fluorescence intensity. If there were two NV$^-$ of different orientation the off-axis magnetic field would further suppress the counts from one of them. Finally, multiple HBT measurements were taken with and without an aligned magnetic field and there was no clear difference in the $g^{(2)}(0)$ value between the two cases. Once again, if there were two NV$^-$ of different orientation the magnetic field should change the level of suppression of the emission from one of the NV$^-$, changing the $g^{(2)}(0)$ value.

Secondly, if one of the two NV$^-$ is charge switching to NV^0 then its average fluorescence intensity is reduced. However, step changes in count rate due to charge state switching have never been observed for ND1. It could be that charge switching is happening at a high frequency that cannot be seen as step changes in the fluorescence count rate, however, the charge switching would have had to have been consistently high frequency over the many hours of ND1 observations.
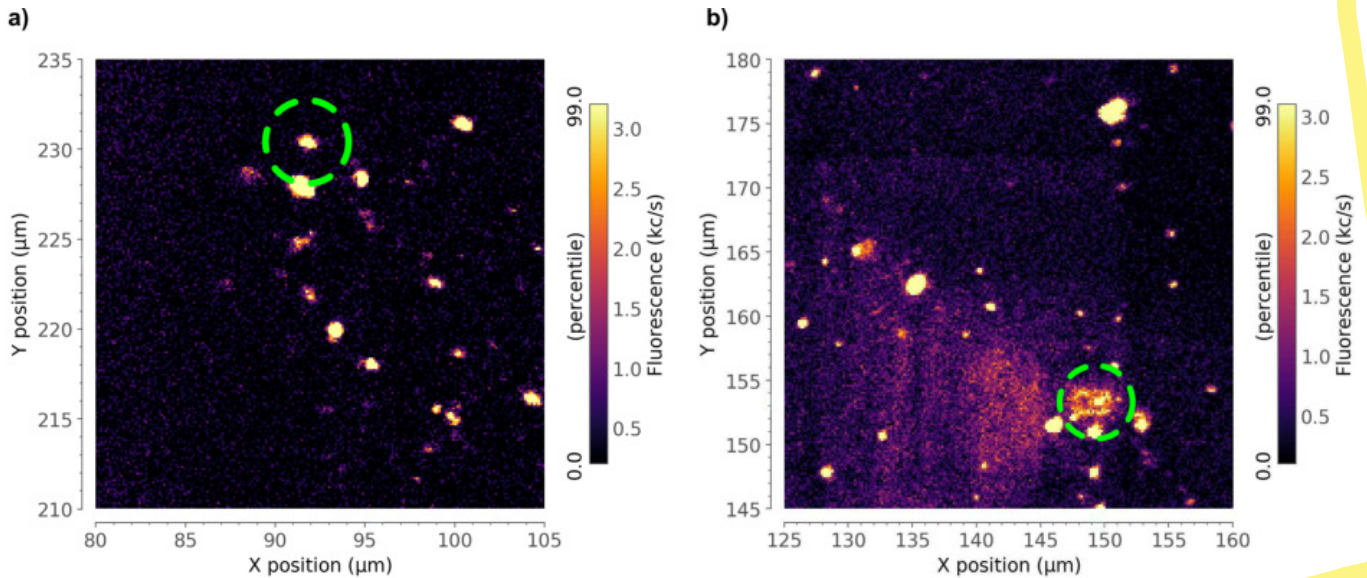
FIG. 5. Confocal fluorescence microscopy (CFM) images of ND1 identified by a green (light gray) dashed ring. (a) CFM taken prior to scanning electron microscopy (SEM) observation of ND1. (b) CFM taken after SEM observation of ND1. A bright rectangle of background fluorescence is visible surrounding ND1. This background is not present prior to SEM observation. Images plotted using the Qudi software suite [45].

Finally, high background count levels can inflate $g^{(2)}(0)$ values by increasing the number of coincident counts. For ND1, dynamical decoupling measurements were taken after the sample had been observed by SEM. After SEM, a rectangle of background fluorescence, more intense than the global background, was visible around ND1, as shown in Fig. 5. It is possible that the electron dose incident on the silicon on which ND1 sits caused fluorescent material to electrostatically stick to the silicon around ND1. Furthermore a HBT measurement taken prior to SEM observation gave a value of $g^{(2)}(0) = 0.21 \pm 0.11$.

Therefore, despite the inflated value for an ideal single NV$^-$ center, $g^{(2)}(0) = 0.39 \pm 0.02$, secondary observations and the $g^{(2)}(0) < 0.5$ condition being satisfied suggest that ND1 is a nanodiamond containing a single NV$^-$ in the presence of a high level of background counts.

Appendix C: ^{13}C revivals

Dynamical decoupling sequences, such as Hahn echo and XY8-n, act to cancel magnetic fluctuations local to the NV$^-$ center that are static, or change slowly with respect to the π pulse spacing. However, a prominent dynamical change in the magnetic environment is due to the precession of ^{13}C spins. Slight differences in the precession frequency of ^{13}C spins in the surrounding spin bath due to slight misalignment between the external magnetic field and the NV$^-$ axis and hyperfine interaction between those spins and the NV$^-$ spin induces decoherence [54].

Alongside the decoherence effects of the ^{13}C spin bath, individual ^{13}C spins close to the NV$^-$ can couple co-herently through the hyperfine interaction causing collapses and revivals in the fluorescence intensity in spin-echo measurements [53, 55]. Examples of these collapses and revivals are shown in Fig. 6 in a Hahn echo measurement on ND1, where the oscillation is well described by the interaction between the NV$^-$ and one proximal ^{13}C spin.

The revivals are not present in Fig. 3 of the main text as the sampled evolution times are chosen to match the peaks of the revivals in the spin-echo signal. This allows the measurement to be run with far fewer data points than would be required to adequately fit the oscillations across the full $0-400$ μs range. The exponential envelope, and as such the T_2 times, can then be fit with a higher signal-to-noise ratio for the same elapsed time as each data point can be repeated a greater number of times.

For the longer pulses sequences, XY8-1 and XY8-4, the time required to collect enough data points with a good enough signal-to-noise ratio to properly fit the revivals becomes prohibitive. Therefore, the sampled evolution times are chosen to match the revival peaks once again. However, the minimum inter-pulse wait time, $\frac{\tau}{2}$, in Fig. 3(b) of the main text must be an integer multiple of the revival time. This integer requirement to hit the revival peaks means that the total evolution time in XY8-4 steps in integer multiples of 32 times the fitted revival period in Fig. 3. This is why there are only seven points in the XY8-4 measurement in Fig. 3(a) of the main text, as that is the most tightly spaced evolution time sampling possible whilst still hitting revival peaks.
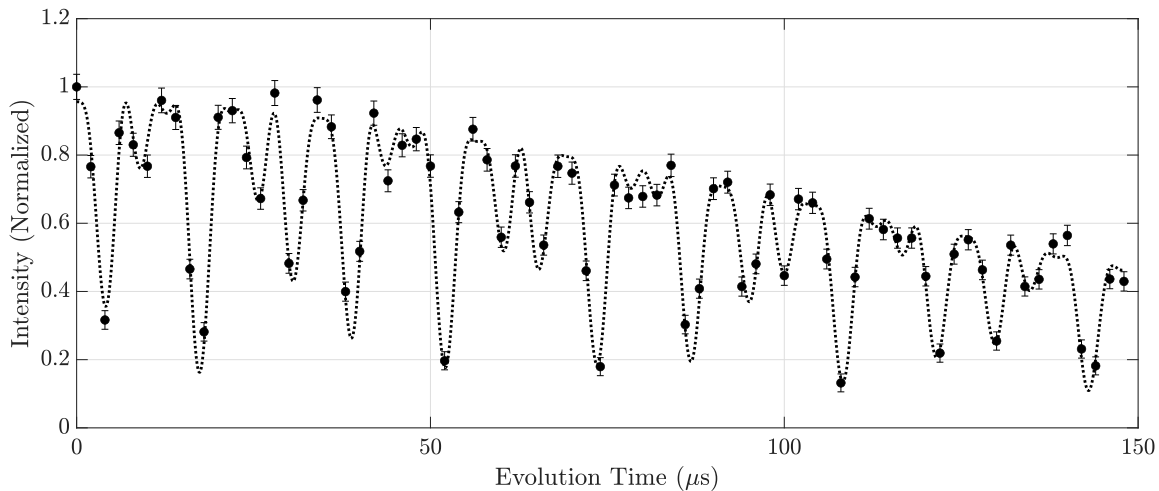
FIG. 6. Hahn echo measurement of ND1 with shorter inter-point spacing than in Fig. 3 of the main text. Revivals in spin-echo signal due to ^{13}C spins are well fit by $a + b\exp\left[-(t/T_2)^n\right]\left(1 - c\,\sin\left(\frac{\pi t}{d}\right)^2\sin\left(\frac{\pi t}{g}\right)^2\right)$ [53, 55]. Where $d = 6.975 \pm 0.007$ µs and $g = 11.44 \pm 0.02$ µs.
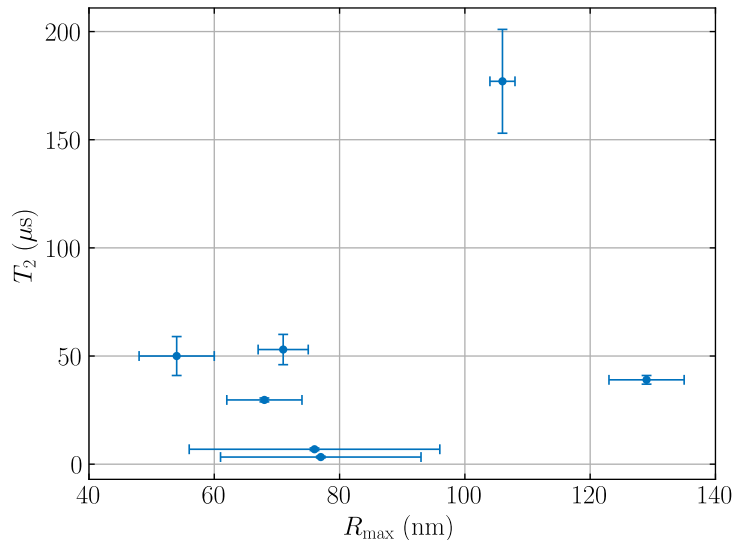

FIG. 7. Spin echo T_2 times against the estimated maximum distance the NV$^-$ could be from the surface ($R_{\max}$), plotted for all seven nanodiamonds that contained an NV$^-$ for which a T_2 was measured.

Appendix D: Nanodiamond size vs. T_2 time

Using the grid markings etched onto the silicon the nanodiamonds are deposited on, each nanodiamond that contained an NV$^-$ for which a T_2 was measured was viewed under SEM. Fig. 7 shows that we did not observe a correlation between nanodiamond size and T_2 time.

There are limitations to characterizing the nanodiamond size under SEM. The two dimensional image allows the projected size to be measured, but provides no information as to the depth of the nanodiamond. Nanodiamonds are sometimes deposited in clumps, leaving it unclear under SEM as to whether there is one large nanodiamond that contains the NV$^-$, or a smaller nanodiamond containing the NV$^-$ next to another small nanodiamond that does not contain an NV$^-$. This is the case for the two data points in Fig. 7 that have $T_2 < 10$ µs.

Even if the SEM observations could provide perfect information on the size and shape of each nanodiamond, we have no knowledge of the location of the NV$^-$ center within the diamond. Therefore, $R_{\max}$ is an estimate from the SEM images of the maximum distance that the NV$^-$ center could be from the surface. These factors, along with those discussed in the main text, all contribute to mask any possible correlation between the nanodiamond size and T_2 time.

[1] M. W. Doherty, N. B. Manson, P. Delaney, F. Jelezko, J. Wrachtrup, and L. C. L. Hollenberg, The nitrogen-vacancy colour centre in diamond, Phys. Rep. **528**, 1 (2013).

[2] L. Robledo, L. Childress, H. Bernien, B. Hensen, P. F. A. Alkemade, and R. Hanson, High-fidelity projective readout of a solid-state spin quantum register, Nature **477**, 574 (2011).

[3] C. E. Bradley, J. Randall, M. H. Abobeih, R. C. Berrevoets, M. J. Degen, M. A. Bakker, M. Markham, D. J. Twitchen, and T. H. Taminiau, A Ten-Qubit Solid-State Spin Register with Quantum Memory up to One Minute, Phys. Rev. X **9**, 031045 (2019).

[4] L. Rondin, J.-P. Tetienne, T. Hingant, J.-F. Roch, P. Maletinsky, and V. Jacques, Magnetometry with nitrogen-vacancy defects in diamond, Rep. Prog. Phys. **77**, 056503 (2014).

[5] J. F. Barry, J. M. Schloss, E. Bauch, M. J. Turner, C. A. Hart, L. M. Pham, and R. L. Walsworth, Sensitivity optimization for NV-diamond magnetometry, Rev. Mod. Phys. **92**, 015004 (2020).

[6] F. Dolde, H. Fedder, M. W. Doherty, T. Nöbauer, F. Rempp, G. Balasubramanian, T. Wolf, F. Reinhard, L. C. L. Hollenberg, F. Jelezko, and J. Wrachtrup, Electric-field sensing using single diamond spins, Nat. Phys. **7**, 459 (2011).

[7] F. Dolde, M. W. Doherty, J. Michl, I. Jakobi, B. Naydenov, S. Pezzagna, J. Meijer, P. Neumann, F. Jelezko, N. B. Manson, and J. Wrachtrup, Nanoscale Detection of a Single Fundamental Charge in Ambient Conditions Using the NV- Center in Diamond, Phys. Rev. Lett. **112**, 097603 (2014).

[8] S. Karaveli, O. Gaathon, A. Wolcott, R. Sakakibara, O. A. Shemesh, D. S. Peterka, E. S. Boyden, J. S. Owen, R. Yuste, and D. Englund, Modulation of nitrogen vacancy charge state and fluorescence in nanodiamonds using electrochemical potential, Proc. Natl. Acad. Sci. U.S.A. **113**, 3938 (2016).

[9] E. H. Chen, H. A. Clevenson, K. A. Johnson, L. M. Pham, D. R. Englund, P. R. Hemmer, and D. A. Braje, High-sensitivity spin-based electrometry with an ensemble of nitrogen-vacancy centers in diamond, Phys. Rev. A **95**, 053417 (2017).

[10] V. M. Acosta, E. Bauch, M. P. Ledbetter, A. Waxman, L. S. Bouchard, and D. Budker, Temperature Dependence of the Nitrogen-Vacancy Magnetic Resonance in Diamond, Phys. Rev. Lett. **104**, 070801 (2010).

[11] D. M. Toyli, C. F. de las Casas, D. J. Christle, V. V. Dobrovitski, and D. D. Awschalom, Fluorescence thermometry enhanced by the quantum coherence of single spins in diamond, Proc. Natl. Acad. Sci. U.S.A. **110**, 8417 (2013).

[12] P. Neumann, I. Jakobi, F. Dolde, C. Burk, R. Reuter, G. Waldherr, J. Honert, T. Wolf, A. Brunner, J. H. Shim, D. Suter, H. Sumiya, J. Isoya, and J. Wrachtrup, High-Precision Nanoscale Temperature Sensing Using Single Defects in Diamond, Nano Lett. **13**, 2738 (2013).

[13] T. Plakhotnik, M. W. Doherty, J. H. Cole, R. Chapman, and N. B. Manson, All-Optical Thermometry and Thermal Properties of the Optically Detected Spin Resonances of the NV-Center in Nanodiamond, Nano Lett.

[14] **14**, 4989 (2014).

[14] F. Jelezko and J. Wrachtrup, Single defect centres in diamond: A review, Phys. Status Solidi A **203**, 3207 (2006).

[15] S.-J. Yu, M.-W. Kang, H.-C. Chang, K.-M. Chen, and Y.-C. Yu, Bright fluorescent nanodiamonds: No photobleaching and low cytotoxicity, J. Am. Chem. Soc. **127**, 17604 (2005).

[16] C. C. Fu, H. Y. Lee, K. Chen, T. S. Lim, H. Y. Wu, P. K. Lin, P. K. Wei, P. H. Tsao, H. C. Chang, and W. Fann, Characterization and application of single fluorescent nanodiamonds as cellular biomarkers, Proc. Natl. Acad. Sci. U.S.A. **104**, 727 (2007).

[17] F. Neugart, A. Zappe, F. Jelezko, C. Tietz, J. P. Boudou, A. Krueger, and J. Wrachtrup, Dynamics of Diamond Nanoparticles in Solution and Cells, Nano Lett. **7**, 3588 (2007).

[18] Y.-R. Chang, H.-Y. Lee, K. Chen, C.-C. Chang, D.-S. Tsai, C.-C. Fu, T.-S. Lim, Y.-K. Tzeng, C.-Y. Fang, C.-C. Han, H.-C. Chang, and W. Fann, Mass production and dynamic imaging of fluorescent nanodiamonds, Nat. Nanotechnol. **3**, 486 (2008).

[19] L. P. McGuinness, Y. Yan, A. Stacey, D. A. Simpson, L. T. Hall, D. MacLaurin, S. Prawer, P. Mulvaney, J. Wrachtrup, F. Caruso, R. E. Scholten, and L. C. L. Hollenberg, Quantum measurement and orientation tracking of fluorescent nanodiamonds inside living cells, Nat. Nanotechnol. **6**, 358 (2011).

[20] A. Schroeder, D. A. Heller, M. M. Winslow, J. E. Dahlman, G. W. Pratt, R. Langer, T. Jacks, and D. G. Anderson, Treating metastatic cancer with nanotechnology, Nat. Rev. Cancer **12** (2012).

[21] D. Le Sage, K. Arai, D. R. Glenn, S. J. Devience, L. M. Pham, L. Rahn-Lee, M. D. Lukin, A. Yacoby, A. Komeili, and R. L. Walsworth, Optical magnetic imaging of living cells, Nature **496**, 486 (2013).

[22] G. Kucsko, P. C. Maurer, N. Y. Yao, M. Kubo, H. J. Noh, P. K. Lo, H. Park, and M. D. Lukin, Nanometre-scale thermometry in a living cell, Nature **500**, 54 (2013).

[23] M. Chipaux, K. J. van der Laan, S. R. Hemelaar, M. Hasani, T. Zheng, and R. Schirhagl, Nanodiamonds and their applications in cells, Small **14**, 1704263 (2018).

[24] P. Wang, S. Chen, M. Guo, S. Peng, M. Wang, M. Chen, W. Ma, R. Zhang, J. Su, X. Rong, F. Shi, T. Xu, and J. Du, Nanoscale magnetic imaging of ferritins in a single cell, Sci. Adv. **5**, eaau8038 (2019).

[25] J. Choi, H. Zhou, R. Landig, H.-Y. Wu, X. Yu, S. E. Von Stetina, G. Kucsko, S. E. Mango, D. J. Needleman, A. D. T. Samuel, P. C. Maurer, H. Park, and M. D. Lukin, Probing and manipulating embryogenesis via nanoscale thermometry and temperature control, Proc. Natl. Acad. Sci. U.S.A. **117**, 14636 (2020).

[26] M. Fujiwara, S. Sun, A. Dohms, Y. Nishimura, K. Suto, Y. Takezawa, K. Oshimi, L. Zhao, N. Sadzak, Y. Umehara, Y. Teki, N. Komatsu, O. Benson, Y. Shikano, and E. Kage-Nakadai, Real-time nanodiamond thermometry probing in vivo thermogenic responses, Sci. Adv. **6**, eaba9636 (2020).

[27] M. Scala, M. S. Kim, G. W. Morley, P. F. Barker, and S. Bose, Matter-Wave Interferometry of a Levitated Thermal Nano-Oscillator Induced and Probed by a Spin, Phys. Rev. Lett. **111**, 180403 (2013).

[28] Z.-q. Yin, T. Li, X. Zhang, and L. M. Duan, Large quantum superpositions of a levitated nanodiamond through spin-optomechanical coupling, Phys. Rev. A **88**, 033614 (2013).

[29] C. Wan, M. Scala, G. W. Morley, ATM. A. Rahman, H. Ulbricht, J. Bateman, P. F. Barker, S. Bose, and M. S. Kim, Free Nano-Object Ramsey Interferometry for Large Quantum Superpositions, Phys. Rev. Lett. **117**, 143003 (2016).

[30] C. Wan, M. Scala, S. Bose, A. C. Frangeskou, ATM. A. Rahman, G. W. Morley, P. F. Barker, and M. S. Kim, Tolerance in the Ramsey interference of a trapped nanodiamond, Phys. Rev. A **93**, 043852 (2016).

[31] J. S. Pedernales, G. W. Morley, and M. B. Plenio, Motional dynamical decoupling for interferometry with macroscopic particles, Phys. Rev. Lett. **125**, 023602 (2020).

[32] B. D. Wood, S. Bose, and G. W. Morley, Spin dynamical decoupling for generating macroscopic superpositions of a free-falling nanodiamond, Phys. Rev. A **105**, 012824 (2022).

[33] A. Albrecht, A. Retzker, and M. B. Plenio, Testing quantum gravity by nanodiamond interferometry with nitrogen-vacancy centers, Phys. Rev. A **90**, 033834 (2014).

[34] S. Bose, A. Mazumdar, G. W. Morley, H. Ulbricht, M. Toroš, M. Paternostro, A. A. Geraci, P. F. Barker, M. S. Kim, and G. Milburn, Spin Entanglement Witness for Quantum Gravity, Phys. Rev. Lett. **119**, 240401 (2017).

[35] C. Marletto and V. Vedral, Gravitationally Induced Entanglement between Two Massive Particles is Sufficient Evidence of Quantum Effects in Gravity, Phys. Rev. Lett. **119**, 240402 (2017).

[36] M. H. Abobeih, J. Cramer, M. A. Bakker, N. Kalb, M. Markham, D. J. Twitchen, and T. H. Taminiau, One-second coherence for a single electron spin coupled to a multi-qubit nuclear-spin environment, Nat. Commun. **9**, 2552 (2018).

[37] N. Bar-Gill, L. M. Pham, A. Jarmola, D. Budker, and R. L. Walsworth, Solid-state electronic spin coherence time approaching one second, Nat. Commun. **4**, 1743 (2013).

[38] G. Balasubramanian, P. Neumann, D. Twitchen, M. Markham, R. Kolesov, N. Mizuochi, J. Isoya, J. Achard, J. Beck, J. Tissler, V. Jacques, P. R. Hemmer, F. Jelezko, and J. Wrachtrup, Ultralong spin coherence time in isotopically engineered diamond, Nat. Mater. **8**, 383 (2009).

[39] P. Andrich, B. J. Alemán, J. C. Lee, K. Ohno, C. F. de las Casas, F. J. Heremans, E. L. Hu, and D. D. Awschalom, Engineered Micro- and Nanoscale Diamonds as Mobile Probes for High-Resolution Sensing in Fluid, Nano Lett. **14**, 4959 (2014).

[40] M. E. Trusheim, L. Li, A. Laraoui, E. H. Chen, H. Bakhru, T. Schröder, O. Gaathon, C. A. Meriles, and D. Englund, Scalable Fabrication of High Purity Diamond Nanocrystals with Long-Spin-Coherence Nitrogen Vacancy Centers, Nano Lett. **14**, 32 (2014).

[41] H. S. Knowles, D. M. Kara, and M. Atatüre, Observing bulk diamond spin coherence in high-purity nanodiamonds, Nat. Mater. **13**, 21 (2014).

[42] L. Rondin, G. Dantelle, A. Slablab, F. Grosshans, F. Treussart, P. Bergonzo, S. Perruchas, T. Gacoin, M. Chaigneau, H.-C. Chang, V. Jacques, and J.-F. Roch, Surface-induced charge state conversion of nitrogen-vacancy defects in nanodiamonds, Phys. Rev. B **82**, 115449 (2010).

[43] S. Sangtawesin, B. L. Dwyer, S. Srinivasan, J. J. Allred, L. V. H. Rodgers, K. De Greve, A. Stacey, N. Dontschuk, K. M. O'Donnell, D. Hu, D. A. Evans, C. Jaye, D. A. Fischer, M. L. Markham, D. J. Twitchen, H. Park, M. D. Lukin, and N. P. de Leon, Origins of Diamond Surface Noise Probed by Correlating Single-Spin Measurements with Surface Spectroscopy, Phys. Rev. X **9**, 031052 (2019).

[44] T. de Guillebon, B. Vindolet, J.-F. Roch, V. Jacques, and L. Rondin, Temperature dependence of the longitudinal spin relaxation time T_1 of single nitrogen-vacancy centers in nanodiamonds, Phys. Rev. B **102**, 165427 (2020).

[45] J. M. Binder, A. Stark, N. Tomek, J. Scheuer, F. Frank, K. D. Jahnke, C. Müller, S. Schmitt, M. H. Metsch, T. Unden, T. Gehring, A. Huck, U. L. Andersen, L. J. Rogers, and F. Jelezko, Qudi: A modular python suite for experiment control and data processing, SoftwareX **6**, 85 (2017).

[46] A. C. Frangeskou, A. T. M. A. Rahman, L. Gines, S. Mandal, O. A. Williams, P. F. Barker, and G. W. Morley, Pure nanodiamonds for levitated optomechanics in vacuum, New J. Phys. **20**, 043016 (2018).

[47] A. M. Edmonds, U. F. S. D'Haenens-Johansson, R. J. Cruddace, M. E. Newton, K. M. C. Fu, C. Santori, R. G. Beausoleil, D. J. Twitchen, and M. L. Markham, Production of oriented nitrogen-vacancy color centers in synthetic diamond, Phys. Rev. B **86**, 035201 (2012).

[48] L. Ginés, S. Mandal, D. J. Morgan, R. Lewis, P. R. Davies, P. Borri, G. W. Morley, and O. A. Williams, Production of metal-free diamond nanoparticles, ACS Omega **3**, 16099 (2018).

[49] Y. Chu, N. P. de Leon, B. J. Shields, B. Hausmann, R. Evans, E. Togan, M. J. Burek, M. Markham, A. Stacey, A. S. Zibrov, A. Yacoby, D. J. Twitchen, M. Loncar, H. Park, P. Maletinsky, and M. D. Lukin, Coherent Optical Transitions in Implanted Nitrogen Vacancy Centers, Nano Lett. **14**, 1982 (2014).

[50] J. Hees, A. Kriele, and O. A. Williams, Electrostatic self-assembly of diamond nanoparticles, Chem. Phys. Lett. **509**, 12 (2011).

[51] T. M. Babinec, B. J. M. Hausmann, M. Khan, Y. Zhang, J. R. Maze, P. R. Hemmer, and M. Lončar, A diamond nanowire single-photon source, Nat. Nanotechnol. **5**, 195 (2010).

[52] S. A. Momenzadeh, R. J. Stöhr, F. F. de Oliveira, A. Brunner, A. Denisenko, S. Yang, F. Reinhard, and J. Wrachtrup, Nanoengineered Diamond Waveguide as a Robust Bright Platform for Nanomagnetometry Using Shallow Nitrogen Vacancy Centers, Nano Lett. **15**, 165 (2015).

[53] J. R. Maze, J. M. Taylor, and M. D. Lukin, Electron spin decoherence of single nitrogen-vacancy defects in diamond, Phys. Rev. B **78**, 094303 (2008).

[54] P. L. Stanwix, L. M. Pham, J. R. Maze, D. Le Sage, T. K. Yeung, P. Cappellaro, P. R. Hemmer, A. Yacoby, M. D. Lukin, and R. L. Walsworth, Coherence of nitrogen-vacancy electronic spin ensembles in diamond, Phys. Rev. B **82**, 201201(R) (2010).

[55] L. Childress, M. V. G. Dutt, J. M. Taylor, A. S. Zibrov, F. Jelezko, J. Wrachtrup, P. R. Hemmer, and M. D.

Lukin, Coherent Dynamics of Coupled Electron and Nuclear Spin Qubits in Diamond, Science **314**, 281 (2006).

[56] S. B. van Dam, M. Walsh, M. J. Degen, E. Bersin, S. L. Mouradian, A. Galiullin, M. Ruf, M. IJspeert, T. H. Taminiau, R. Hanson, and D. R. Englund, Optical coherence of diamond nitrogen-vacancy centers formed by ion implantation and annealing, Phys. Rev. B **99**, 161203(R) (2019).

[57] T. M. Hoang, J. Ahn, J. Bang, and T. Li, Electron spin control of optically levitated nanodiamonds in vacuum, Nat. Commun. **7**, 12250 (2016).

[58] J.-F. Hsu, P. Ji, C. W. Lewandowski, and B. D'Urso, Cooling the Motion of Diamond Nanocrystals in a Magneto-Gravitational Trap in High Vacuum, Sci. Rep. **6**, 30125 (2016).

[59] R. M. Pettit, L. P. Neukirch, Y. Zhang, and A. Nick Vamivakas, Coherent control of a single nitrogen-vacancy center spin in optically levitated nanodiamond, J. Opt. Soc. Am. B **34**, C31 (2017).

[60] T. Delord, P. Huillery, L. Schwab, L. Nicolas, L. Lecordier, and G. Hétet, Ramsey Interferences and Spin Echoes from Electron Spins Inside a Levitating Macroscopic Particle, Phys. Rev. Lett. **121**, 053602 (2018).

[61] G. P. Conangla, A. W. Schell, R. A. Rica, and R. Quidant, Motion Control and Optical Interrogation of a Levitating Single Nitrogen Vacancy in Vacuum, Nano Lett. **18**, 3956 (2018).

[62] M. C. O'Brien, S. Dunn, J. E. Downes, and J. Twamley, Magneto-mechanical trapping of micro-diamonds at low pressures, Appl. Phys. Lett. **114**, 053103 (2019).